— 12 —

In-flight Calibration of the UVCS White Light Channel

MARCO ROMOLI
Dip. di Astronomia e Scienza dello Spazio, Università di Firenze, Firenze, Italy

RICHARD A. FRAZIN, JOHN L. KOHL,
LARRY D. GARDNER, STEVEN R. CRANMER
Harvard-Smithsonian Center for Astrophysics, Cambridge, MA, USA

KEVIN REARDON
Dip. di Astronomia e Scienza dello Spazio, Università di Firenze, Firenze, Italy

SILVANO FINESCHI
Osservatorio Astronomico di Torino, Pino Torinese, Italy

The UVCS White Light Channel (WLC) is designed to measure the linearly polarized radiance (pB) of the corona, in the wavelength band from 450 nm to 600 nm, in order to derive one of the fundamental parameters of the solar corona: the electron density. This paper gives a thorough description of the in-flight radiometric calibration of the WLC, which uses the star α Leo and the planet Jupiter as transfer standards and is based on calibrations of ground-based instruments. The method for computing the polarized radiance from the measurements is also described, together with the stray light and polarization characterizations obtained from dedicated, in-flight measurements.

12.1 Instrument Description

The UVCS/WLC is discussed extensively in *Romoli* [1992] , *Romoli et al.* [1993], and *Kohl et al.* [1995]. The UVCS/WLC is designed to measure the linearly polarized radiance of the corona in the band from 450 nm to 600 nm. Figure 12.1 is a schematic diagram of the UVCS/WLC telescope layout. Like the UV channels, the WLC is an internally- and externally-occulted coronagraph. The primary mirror focuses the coronal light onto the entrance pinhole. This pinhole corresponds to a $14''$ by $14''$ patch of sky. Figure 12.2 is a schematic diagram of the part of the WLC that lies beyond the entrance pinhole. The light diverges from the pinhole and first passes through a rotating, half-wave retarder plate (HWRP), which rotates the plane of linear polarization. Next, the light passes through a fixed linear polarizer, which allows only the component with the electric field vector oscillating in a specific direction to pass through. The amount of light transmitted depends on the angle between the plane of polarization of the incident light and the transmission axis of the polarizer. Choosing three different rotation angles of the HWRP allows one to

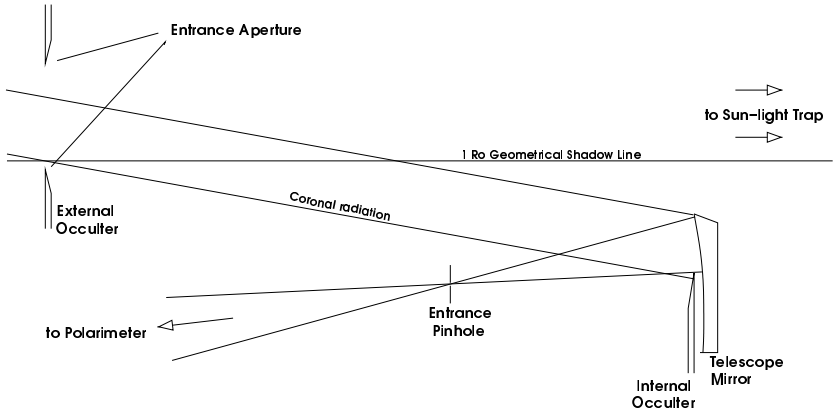

Figure 12.1: Schematic diagram of the UVCS/WLC telescope layout (not to scale).

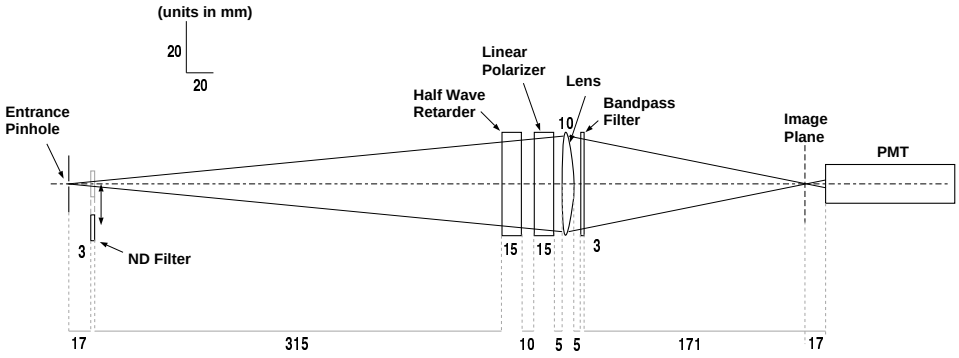

Figure 12.2: Schematic diagram of the UVCS/WLC polarimeter. Taken from *Kohl et al.* [1995].

determine the Stokes I, Q and U components, which is the linear polarization (see Section 12.2). After passing through the polarizer the light goes through a spherical lens and a bandpass filter (450 nm to 600 nm). The spherical lens forms an image of the pinhole just in front of the detector and the bandpass filter controls the spectral properties of the light. Since the linear polarizer is fixed, the light that passes through the lens and the bandpass filter and hits the detector is always 100 % linearly polarized in the same way, regardless of the observation. This makes the characterization of the optical system simpler. The detector is a photomultiplier tube (PMT) designed to work in photon counting mode.

12.2 Polarization Measurement

The polarization state of partially polarized light is most readily described by the vector of Stokes parameters, $\boldsymbol{s} = [s_I, s_Q, s_U, s_V]^T$, where ^{T} denotes the transpose operator.

Although *Collett* [1993] describes this elementary material in detail, we review it here. The Stokes vector $\boldsymbol{s} = [s_I, s_Q, s_U, s_V]^T$ has units of photon spectral radiance such as $\mathrm{cm}^{-2}\ \mathrm{s}^{-1}\ \mathrm{sr}^{-1}\ \mathrm{nm}^{-1}$. The I component is the total spectral radiance of the light including the polarized and unpolarized components. If the light is completely polarized $s_I = \sqrt{s_Q^2 + s_U^2 + s_V^2}$, and if the light is partially polarized $s_I > \sqrt{s_Q^2 + s_U^2 + s_V^2}$. For a given coordinate system, the Q component corresponds to horizontal (parallel to the x-axis) linear polarization if $s_Q > 0$ and vertical linear polarization if $s_Q < 0$. The U component corresponds to $+45°$ linear polarization if $s_U > 0$ and $-45°$ linear polarization if $s_U < 0$. The V component corresponds to right-circular polarization if $s_V > 0$ and left-circular polarization if $s_V < 0$. The angle of the plane linear polarization ψ is given by the relation $\tan 2\psi = s_U/s_Q$. Light that is elliptically polarized may have nonzero values for all four components of the Stokes vector.

The light from the solar disk Thompson scatters off the free electrons in the corona, and this scattered light is partially polarized [*Collett*, 1993] with the electric field vector of the polarized component oscillating tangentially to the solar disk. Given an appropriate coordinate system, the Stokes vector of the light that the corona emits is given by $[s_I, s_Q, 0, 0]^T$, where $s_Q > 0$. s_I and s_Q are related to the distribution of electron density along the line-of-sight (see, e.g., *Altschuler* [1979]). Thus, s_Q is the spectral radiance of the polarized portion of the coronal light. Dust makes a contribution to s_I but not s_Q, at least not within about 5 $\mathrm{R}_\odot$ [*Billings*, 1966].

12.2.1 Polarization Computation

In this section we use the radiometric calibration and the polarization properties of the HWRP and the polarizer to calculate the first three components of the resulting Stokes vector $\boldsymbol{s} = [s_I, s_Q, s_U, s_V]^T$ for a source of arbitrary polarization. As we will see, the UVCS/WLC does not respond to the V component of the Stokes vector.

The effects of polarizing components in an optical system can be described using Mueller matrices. The Mueller matrices for retarder plates and polarizers as a function of rotation angle may be found in *Collett* [1993]. We will take the x-axis to be parallel to the occulter edge. The Mueller matrix for a HWRP with the fast axis rotated by an angle α relative to the x-axis is $\boldsymbol{M}_R(\alpha) = \boldsymbol{R}(-2\alpha)\boldsymbol{M}_R(0)\boldsymbol{R}(2\alpha)$, where $\boldsymbol{R}$ and $\boldsymbol{M}_R(0)$ are the Mueller matrices for rotation and a HWRP at $\alpha = 0$, respectively. The angle α in the $\boldsymbol{R}$ matrix is multiplied by two because the rotated Stokes vector, which is an intensity vector, is the product of the rotated electric-field vector and its complex conjugate. We have

$$\boldsymbol{M}_R(\alpha) = \begin{pmatrix} 1 & 0 & 0 & 0 \\ 0 & \cos 4\alpha & \sin 4\alpha & 0 \\ 0 & \sin 4\alpha & -\cos 4\alpha & 0 \\ 0 & 0 & 0 & -1 \end{pmatrix} \tag{12.1}$$

where the overall responsivity factor is set to unity (see below).

The Mueller matrix for an ideal polarizer with a fast axis at an angle β to the x direction is given by $\boldsymbol{M}_P(\beta) = \boldsymbol{R}(-2\beta)\boldsymbol{M}_P(0)\boldsymbol{R}(2\beta)$, where $\boldsymbol{R}$ and $\boldsymbol{M}_P(0)$ are the Mueller matrices for rotation and a linear polarizer at $\beta = 0$, respectively. Again, the angle β in the $\boldsymbol{R}$ matrix is multiplied by two because the Stokes vector is a vector of intensities, not

fields. We have

$$\boldsymbol{M}_P(\beta) \;=\; \frac{1}{2}\begin{pmatrix} 1 & \cos 2\beta & \sin 2\beta & 0 \\ \cos 2\beta & \cos^2 2\beta & \cos 2\beta \sin 2\beta & 0 \\ \sin 2\beta & \cos 2\beta \sin 2\beta & \sin^2 2\beta & 0 \\ 0 & 0 & 0 & 0 \end{pmatrix} \tag{12.2}$$

where the overall responsivity factor is set to unity (see below).

The Stokes vector describing the light after it passes through the HWRP and the polarizer is given by $\boldsymbol{s}' \;=\; \boldsymbol{M}_P(\beta)\boldsymbol{M}_R(\alpha)\boldsymbol{s} \;=\; \boldsymbol{M}(\alpha,\beta)\boldsymbol{s}$. The matrix product is:

$$\boldsymbol{M}(\alpha,\beta) = \frac{1}{2}\begin{pmatrix} 1 & \cos(4\alpha-2\beta) & \sin(4\alpha-2\beta) & 0 \\ \cos(2\beta) & \cos(2\beta)\cos(4\alpha-2\beta) & \cos(2\beta)\sin(4\alpha-2\beta) & 0 \\ \sin(2\beta) & \sin(2\beta)\cos(4\alpha-2\beta) & \sin(2\beta)\sin(4\alpha-2\beta) & 0 \\ 0 & 0 & 0 & 0 \end{pmatrix} \tag{12.3}$$

The value of the polarized spectral radiance s_Q (of which the linearly polarized coronal light is a part) is determined by measuring the count-rates at three rotation angles of the HWRP, α_1, α_2 and α_3. Since the PMT detector signal corresponds to the first element of $\boldsymbol{s}' \;=\; \boldsymbol{M}(\alpha,\beta)\boldsymbol{s}$, only the top row of Equation (12.3) is of consequence for our purposes. For a given position α of the HWRP, the count-rate per nanometer at wavelength λ_0 measured by the detector is

$$N_{\lambda_0}(\alpha) \;=\; \frac{1}{2}C\left(s_I + \cos(4\alpha-2\beta)s_Q + \sin(4\alpha-2\beta)s_U\right)/\mathrm{B}_\odot(\lambda_0) \tag{12.4}$$

where $\mathrm{B}_\odot(\lambda_0)$ is the spectral radiance of the center of the solar disk, and C, which has units s^{-1}, is a scaling factor. C depends on the responsivity, the geometry and the spectral response of the instrument and is described in Section 12.2.3.

12.2.2 WLC Polarization Characterization

Equation (12.4) must be an accurate representation of the observation process if the polarized radiance measurements made by the UVCS/WLC are to be meaningful. Equation (12.4) predicts that the count-rate due to an unpolarized source will not vary with the HWRP angle. Rasters of ρ Leo (done in August 2000) were made at three different HWRP angles. The resulting measurement shows (2 ± 2) % polarization. Since the UVCS/WLC typically measures 0.5 % to 9 % polarized signals, this test was not conclusive. However, later (16 June 2001) measurements of Jupiter show less than 0.5 % polarization.

A report of the tests performed on the flight polarimeter is given in *Pernechele et al.* [1997]. Nearly fully polarized visible light was focused on the entrance pinhole, and the count-rate on the flight PMT was read as the angle of the HWRP was varied.

Ignoring wavelength dependence, efficiencies and geometrical factors, the Stokes vector for a fully linearly polarized signal traveling along the z direction and with the electric field making an angle γ with the x axis is $\boldsymbol{s} = I[1, \cos 2\gamma, \sin 2\gamma, 0]^T$, where I is the total spectral radiance of the beam. Using this Stokes vector in Equation (12.3) to calculate the radiant flux at the PMT gives

$$\hat{R}_F \;=\; \frac{1}{2}I_0\,[1 + \cos(4\alpha - 2\beta - 2\gamma)] \tag{12.5}$$

Equation (12.5) is called the *modulation curve*. This modulation curve describes the results of the white-light laboratory tests of *Romoli and Fineschi* [1993] to a high degree of accuracy. In-flight measurements of the modulation curve using the polarized light of the corona have also been made. An example of such a curve is given in Figure 12.3. In this case Equation (12.5) needs an additional constant term to account for the unpolarized fraction of the light.

In addition, *Frazin* [2002] performed laboratory tests on a replica of the UVCS/WLC polarimeter to verify its characteristics. All tests indicate that the instrument performs as intended.

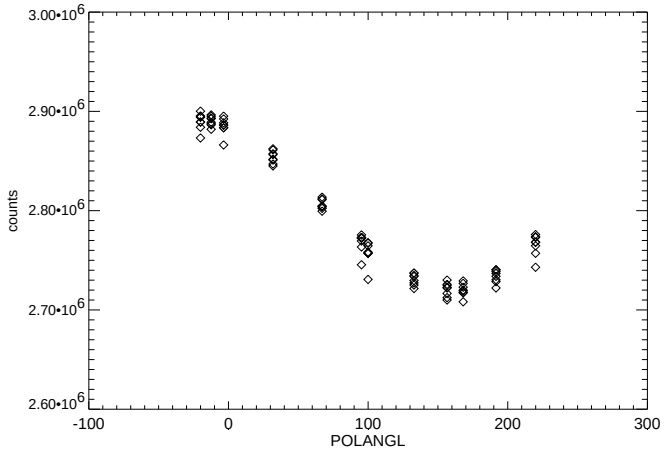

Figure 12.3: In-flight modulation curve. This figure shows the number of PMT counts vs. the UVCS Data Analysis Software (DAS) variable POLANGL $= 4\alpha - 2\beta$ (in deg). This curve was retraced several times and the vertical scatter is caused by time variation of the corona. The data were taken between 19:02 h and 21:15 h on 18 April 1998 at 2.0 $R_\odot$ with 60 s exposures.

12.2.3 WLC Radiometric Factor

The scaling factor, C, contains the radiometric factor that will be derived through the in-flight radiometric calibration. The number of counts per second detected by the PMT per unit wavelength, N_λ, according to Equation (12.4), is

$$\begin{aligned} N_\lambda(r,\alpha) &= R_T \frac{w_p h_p h_m w_m(r)}{f^2} T_L T_P T_F(\lambda)\eta(\lambda) \\ &\quad \times \frac{s_I(\lambda) + s_Q(\lambda)\cos 2\theta + s_U(\lambda)\sin 2\theta}{2} \end{aligned} \tag{12.6}$$

where we have put

$$2\theta = 4\alpha - 2\beta \tag{12.7}$$

and where w_p and h_p are the width and the height of the pinhole (both 50 μm), h_m is the telescope mirror height (3 cm), $w_m(r)$ is the exposed telescope mirror width, f is the mirror focal length (75 cm), R_T is the mirror reflectance, T_L is the lens transmittance and T_P is the polarizer transmittance[1]. $w_m(r)$ in centimeters is given by $0.792r - 0.951 - w_o$ [*Kohl et al.*, 1995], where r is the mirror angle in units of $R_\odot$ (969.6″, as seen from the average SOHO-Sun distance) and w_o is the amount of over-occultation by the internal occulter, 0.15 cm for most observations. The bandpass window spans the wavelength range from 450 nm to 600 nm. The bandpass filter has transmittance $T_F(\lambda)$, and the detected quantum responsivity of the detector system is given by $\eta(\lambda)$. $T_F(\lambda)$ and $\eta(\lambda)$ were measured on the flight units. Plots of $T_F(\lambda)$ and $\eta(\lambda)$ (normalized to unity at 546 nm) are shown in Figure 12.7.

We assume that the spectral distribution of the coronal radiation is the solar Fraunhofer spectrum radiation [*Kurucz et al.*, 1984] convolved with a Gaussian representing a Maxwellian electron velocity distribution corresponding to 10^6 K. Although the F-corona (which shows the Fraunhofer features as they appear on the Sun) and K-corona have different spectra, they differ only by convolution with a function representing the thermal distribution of electron velocities. Since we are integrating the spectrum over a bandpass of ≈150 nm, the convolution is of negligible consequence. Henceforth we ignore the distinctions between the F- and K-corona spectra.

The Stokes vector $\boldsymbol{s}(\lambda, r)$ can be written as $\boldsymbol{s}(\lambda, r) = \mathrm{B}_\odot(\lambda)\boldsymbol{S}(r)$, where $\mathrm{B}_\odot(\lambda)$ is the photospheric photon spectral radiance at Sun center (in units of cm^{-2} sr^{-1} s^{-1} nm^{-1}).[2]

The above assumption makes $\boldsymbol{S}(r)$ wavelength independent. The total count-rate is determined by integrating over the wavelength as follows:

$$N(r,\alpha) = R_T \frac{w_p h_p h_m w_m(r)}{f^2} T_L T_P \left[\int_0^\infty T_F(\lambda)\eta(\lambda)\mathrm{B}_\odot(\lambda)\,\mathrm{d}\lambda\right] \frac{I + Q\cos 2\theta + U\sin 2\theta}{2} \quad (12.8)$$

where we have assumed that T_L, T_P and R_T vary slowly with wavelength over the optical band. We define ϵ to be the value of the responsivity at $\lambda_0 = 546$ nm:

$$\epsilon \equiv \frac{1}{2} R_T\, T_P\, T_L\, T_F(\lambda_0)\, \eta(\lambda_0)\ . \quad (12.9)$$

Using Equations (12.8), (12.7), and (12.9) the total count-rate is:

$$N(r,\alpha) = 2\mathrm{K} w_m(r) \frac{I + Q\cos 2\theta + U\sin 2\theta}{2} \quad (12.10)$$

where

$$\mathrm{K} = \epsilon \frac{w_p h_p h_m}{f^2} \mathrm{B}_\odot(\lambda_0) \left[\int_0^\infty \frac{T_F(\lambda)}{T_F(\lambda_0)} \frac{\eta(\lambda)}{\eta(\lambda_0)} \frac{\mathrm{B}_\odot(\lambda)}{\mathrm{B}_\odot(\lambda_0)} \mathrm{d}\lambda\right] \quad (12.11)$$

In the following sections, the parameters ϵ and K will be called the radiometric responsivity and the WLC radiometric calibration factor, respectively. K is the factor that is used in the UVCS Data Analysis Software (DAS) with the variable name `WLC.VLD.FACTOR`.

[1] Here, the transmittance, T_P, is defined relative to the intensity of a radiation beam which is 100 % linearly polarized along the fast axis. Thus, the transmittance T_P can be ideally 1. This definition requires the dividing factor, 2, in the polarizer Mueller matrix.

[2] Henceforth, we always take $\boldsymbol{S} = [I, Q, U]^T$ to be the Stokes vector in units of photospheric photon spectral radiance at Sun center.

It is clear from Equation (12.10) that the factor C in Equation (12.4) is given by the expression:

$$C = 2\mathrm{K} w_m(r) \tag{12.12}$$

12.3 WLC Radiometric Calibrations

The overall radiometric calibration of the UVCS/WLC is still in progress. This section describes the in-flight radiometric calibration, which is based on observations of the star α Leo and the planet Jupiter. We stress that these are not direct calibrations, rather they use celestial objects as transfer standards and are based on calibrations of ground-based instruments.

Table 12.1 gives a summary of the various in-flight radiometric calibration measurements. All values are in agreement to within the stated standard uncertainties.

method	responsivity
α Leo	(1.16 ± 0.12) %
Jupiter 1997	(1.33 ± 0.13) %
Jupiter 2001	(1.38 ± 0.13) %
mean of α Leo & Jupiter 2001	(1.27 ± 0.09) %

Table 12.1: Radiometric responsivity measurements.

For the purposes of the inter-comparison work presented elsewhere in this volume [*Frazin et al.*, 2002], we adopt the average of the α-Leo and Jupiter 2001 calibrations. Because the pointing scheme was better for the Jupiter 2001 observations, we adopt the Jupiter 2001 calibration as the best value and regard the 1997 result as a confirmation. Thus, the 1997 Jupiter result is not included in the average. The uncertainty associated with the 1997 pointing scheme is not included in Table 12.1.

12.3.1 α-Leo Radiometric Calibration

In August 1998, as part of the UVCS calibration program, we made radiometric measurements of the star α Leo, a B7V star. The α-Leo radiometric calibration is based on literature values of the star's magnitude in the Johnson V band and the catalog of normalized stellar spectra compiled by *Breger* [1976]. Breger's spectra were measured with narrow-band filters. This should be adequate because the library of stellar spectra presented by *Jacoby et al.* [1984] shows that B7V stellar spectra are quite smooth between 400 nm and 650 nm, except for an absorption feature at 486 nm that has a full-width at half-maximum of about 2.3 nm. We used Breger's catalog to determine the shape of the spectra and the V magnitudes from the literature for the normalization. The mean of V magnitudes in the SIMBAD database is 1.36 mag. Accordingly, we calculate the α-Leo photon spectral irradiance at $\lambda_0 = 546$ nm to be $F_{\lambda_0} = 2.91 \times 10^3$ cm^{-2} s^{-1} nm^{-1}. We use the symbol F_λ to represent the irradiance at other wavelengths.

We define $H_{total}(\lambda)$ to be the radiant flux reflected by the mirror. That is,

$$H_{total}(\lambda) = F_\lambda \, h_m \, w_m(r) \, R_T \tag{12.13}$$

where $h_m w_m(r)$ is the exposed mirror area in cm^2, and R_T is the telescope mirror reflectance. $H_{total}(\lambda)$ has units $\mathrm{s}^{-1}\ \mathrm{nm}^{-1}$. The star image in the plane of the pinhole (image plane) is smeared by the telescope optics. We represent this smeared image by the function $\hat{H}(\lambda; x, y)$, where x and y are coordinates in the pinhole plane. The y-axis is defined to be parallel to the internal occulter blade and UV slits (see Figure 12.1). $\hat{H}(\lambda; x, y)$ has units $\mathrm{s}^{-1}\ \mathrm{cm}^{-2}\ \mathrm{nm}^{-1}$ and satisfies the relation

$$H_{total}(\lambda) = \int\int \hat{H}(\lambda; x, y)\,\mathrm{d}x\mathrm{d}y \tag{12.14}$$

If the pinhole is centered at coordinates (x', y') in the pinhole plane, the number of photons per nanometer going through it is given by the expression:

$$H_p(\lambda, x', y') \equiv \int\int \hat{H}(\lambda; x, y)\Pi(\frac{x'-x}{l}, \frac{y'-y}{l})\,\mathrm{d}x\mathrm{d}y \tag{12.15}$$

where $\Pi(x, y)$ is the two-dimensional rectangle function (in each dimension it is unity from -1/2 to 1/2 and zero elsewhere) and l is the width of the (square) pinhole (0.005 cm or 13.76″). The rectangle function $\Pi(x'/l, y'/l)$ represents the square pinhole. H_p has units $\mathrm{s}^{-1}\ \mathrm{nm}^{-1}$. The measured count-rate is proportional to H_p. The rectangle function itself has an area of l^2. Thus, by the properties of the convolution integral in Equation (12.15) and Equation (12.14), we have the relation

$$H_{total}(\lambda) = \frac{1}{l^2}\int\int H_p(\lambda, x, y)\,\mathrm{d}x\mathrm{d}y \tag{12.16}$$

Since the star is unpolarized, the measured count-rate in units of s^{-1} is given by

$$C_r = \frac{1}{2}T_L T_P \int H_p(\lambda, x, y) T_F(\lambda)\eta(\lambda)\mathrm{d}\lambda \tag{12.17}$$

Integrating Equation (12.17) over x and y and using Equations (12.9), (12.13) and (12.16) yields

$$\frac{1}{l^2}\int\int C_r\,\mathrm{d}x\mathrm{d}y = \frac{1}{2}R_T h_m w_m(r) T_L T_P \int F_\lambda T_F(\lambda)\eta(\lambda)\mathrm{d}\lambda \tag{12.18}$$

$$= \epsilon h_m w_m(r) F_{\lambda_0} \int \frac{F_\lambda}{F_{\lambda_0}} \frac{T_F(\lambda)}{T_F(\lambda_0)} \frac{\eta(\lambda)}{\eta(\lambda_0)}\mathrm{d}\lambda \tag{12.19}$$

where ϵ is the radiometric responsivity. Equation (12.18) is similar in form to Equation (12.8). Due to the spectral differences between α Leo and the Sun, it is not useful to incorporate the calibration factor K as in Equation (12.10), although it may be calculated via Equation (12.11) once ϵ is known.

The goal of the α-Leo observation was to determine the responsivity ϵ by making a measurement of the left-hand-side integral in Equation (12.19).

From the perspective of the SOHO spacecraft, stars travel at constant velocity of about $v \approx 0.04''\ \mathrm{s}^{-1}$, or $1.45 \times 10^{-5}\ \mathrm{cm\ s}^{-1}$ in the pinhole plane. For the α-Leo observation, the star trajectory was inclined to the x-axis by 11°. Since $\cos(11°) \approx 0.9816$, this effect is negligible, and for the purpose of this discussion we will assume that the star trajectory is parallel to the x-axis. The observation consisted of eighteen passes. Before each pass the instrument was pointed so that the pinhole was ahead of the star and was not moved

until the entire star image had passed by the pinhole. For each pass, the pinhole was placed so that the star's path was at a different value of the y-coordinate, relative to the pinhole. The value of y was determined from the spatial position of the star's UV signature in the O IV channel. Thus, we may consider the count-rate C_r in Equation (12.17) to be a function of time and y. We will use the notation $C_r(t, y)$ to symbolize this. Using the same proportionality factors as in Equation (12.17), we have the relationship:

$$C_r(t, y) \;\propto\; H_p\,(\lambda; x - v(t - t_0), y) \tag{12.20}$$

where t_0 is chosen so that the maximum count-rate occurs at $t = 0$. Figure 12.4 is an example that shows the time-variation of the count-rate during one pass. The example in the Figure is the first pass, which happened to be near $y = 0$, the center of the pinhole. Integrating $C_r(t, y)$ over time, we may define the quantity

$$\hat{C}_r(y) \equiv \int C_r(t, y)\, v \mathrm{d}t \tag{12.21}$$

$\hat{C}_r(y)$ has units of cm s^{-1}. Numerically integrating the count-rate in each pass gives a measurement of $\hat{C}_r(y)$. We will call $\hat{C}_r(y)$ the *integrated count-rate (ICR)*. $\hat{C}_r(y)$ is related to the responsivity ϵ via Equation (12.19) as follows:

$$\frac{1}{l^2}\int \hat{C}_r(y)\,\mathrm{d}y \;=\; \frac{1}{l^2}\int\int C_r \mathrm{d}x\mathrm{d}y \tag{12.22}$$

The result of the measument is $\epsilon = (1.16 \pm 0.12)$ %. The uncertainty analysis is discussed below.

12.3.2 α-Leo Uncertainty Analysis

The uncertainty in the α-Leo calibration is dominated by the uncertainty in the integration over the y-axis in Equation (12.22). Figure 12.5 shows the results of numerically integrating all of the passes according to Equation (12.21). The statistical uncertainties are negligibly small in the vertical direction because the data from which the integrals in Equation (12.21) were evaluated included millions of counts. The more significant uncertainty is in the y position of each pass, which was determined by fitting a Gaussian to the signal measured in the O VI channel. Each UV signal contained on the order of 2×10^4 counts. The statistical uncertainty in determining the centroid of the Gaussian was much smaller than the overall uncertainty inherent in this procedure. Only the variation of the error in the determination of the individual values of y is important since an overall shift will not affect the integral in the left-hand-side of Equation 12.22. A significant uncertainty is introduced by the fact that the UV spatial image of the star had a full-width at half-maximum of about $25''$ while the spatial binning (3 pixels) was $21''$, and because the spatial image of the star is not a Gaussian, as was assumed by the fitting procedure (rather, it is a point spread function that is not accurately known). We can estimate this uncertainty as one-third of a spatial bin, or $7''$. We consider it to be roughly equivalent to a coverage factor $k = 2$ uncertainty. This $7''$ uncertainty is indicated as horizontal error bars in Figure 12.5.

Although we used spline interpolation of the data points in Figure 12.5 to estimate the left-hand-side integral in Equation (12.22), we chose to model this spatial profile as a sum

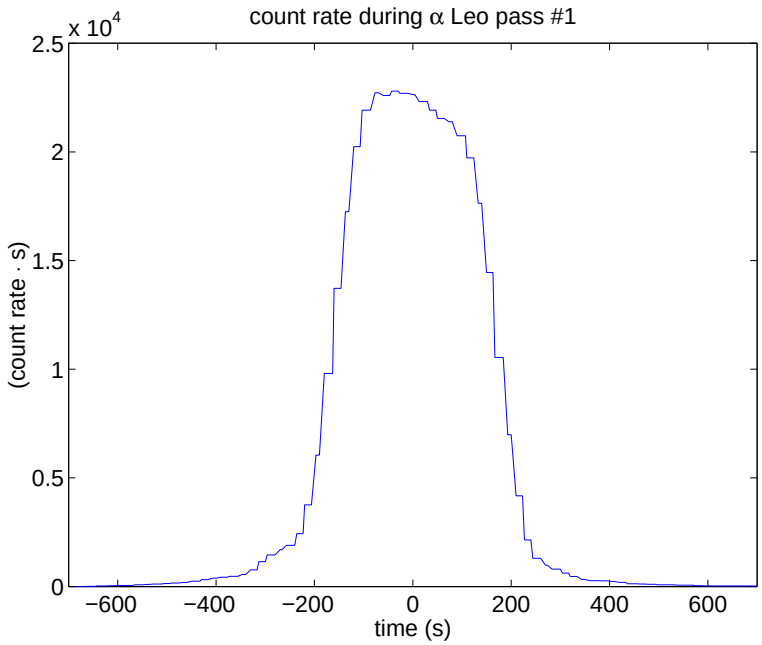

Figure 12.4: The count-rate as a function of time for the first α-Leo pass by the pinhole. The data set consists of a series of such passes.

of two Gaussians for the purposes of the uncertainty analyses of both α Leo and Jupiter, and for computations of the Jupiter broadening function discussed later. The two-Gaussian model can describe the data well, except for two points on the far left of Figure 12.5. We propagated the $7''$ uncertainty through a perturbation analysis in order to determine its effect on the parameters of the two Gaussian model. The result is that the sum of the areas of the two Gaussians has an uncertainty of 20 %. We consider this 20 % uncertainty to be coverage factor $k = 2$ since it is a direct result of the coverage factor $k = 2$ spatial uncertainty discussed above. Therefore, we take the standard uncertainty to be 10 %. The same perturbation analysis allowed us to determine the broadest and narrowest (coverage factor $k = 2$) profiles that are consistent with the data in Figure 12.5; they are shown by the dotted and dashed curves, respectively. These curves will be used later in Section 12.3.4 for the uncertainty analysis in the Jupiter calibration.

The SIMBAD data base shows fourteen V-magnitude measurements of α Leo spanning the years 1952 through 1986. The standard deviation of these measurements is 0.02 mag or 2 %. *Breger* [1976] has nine independent spectrophotometric scans of F_λ. The standard deviation of these normalized spectra is about 0.01 mag between 450 nm and 600 nm. Adding these in quadrature, we find that the determination of F_{λ_0} implies an uncertainty of 2 %.

The uncertainty due to counting statistics in the integrated count rates is negligible. Since the exposed mirror width $w_m(r)$ was 2.56 cm, and the uncertainty in the location of the internal occulter is on the order of 0.01 cm, this effect is also negligible. The curve

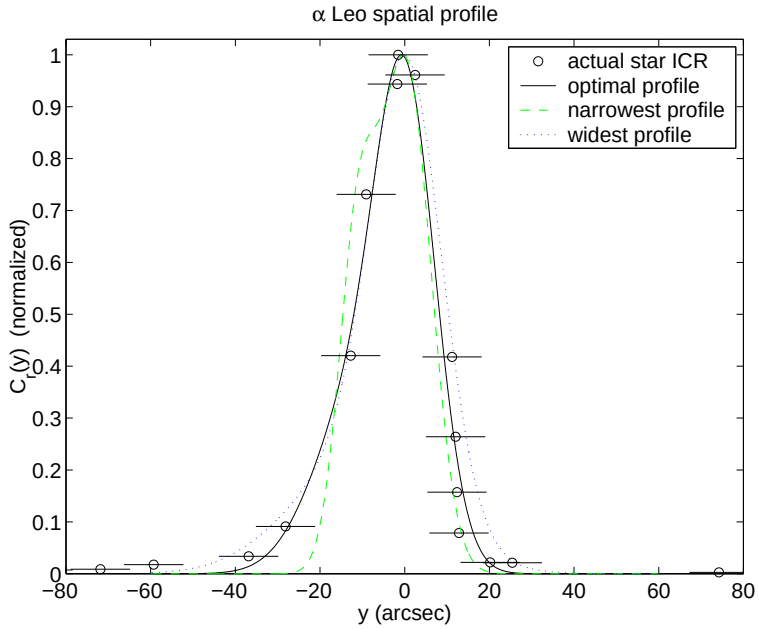

Figure 12.5: The α-Leo integrated count-rate (ICR) along the UV slit (circles) and three point spread function curves to describe it. The $7''$ (coverage factor $k = 2$) uncertainty on the determination of y for each pass is indicated by the horizontal error bars. The solid curve is the optimal one used to calculate the broadening factor in Section 12.3.4. The dotted and dashed curves are the broadest and narrowest functions that the data can justify at the coverage factor $k = 2$ uncertainty level (see text).

$T_F(\lambda)$ was measured in the laboratory on several occasions, to within a few percent. $\eta(\lambda)$ was measured on the flight unit by Ball Aerospace. The $\eta(\lambda)$ measurement agrees with the curve given by the manufacturer. Since the measured responsivity ϵ includes the values of T_F and η at λ_0, any errors in the values of these curves at λ_0 will introduce no uncertainty, although errors in the shapes of these curves can do so. As Figure 12.7 shows, $T_F(\lambda)$ and $\eta(\lambda)$ are smooth curves, so the integral of their normalized product, as is called for in Equation (12.19), does not introduce significant uncertainty. Table 12.2 summarizes this uncertainty analysis.

12.3.3 ρ-Leo Consistency Check

In August 1998, as part of the UVCS calibration program, we made radiometric measurements of the star ρ Leo. According to *Breger* [1976] and the SIMBAD data base, the ρ-Leo flux at 546 nm is 9.9 % that of α Leo and its $F_\lambda / F_{\lambda_0}$ curve is nearly identical in the UVCS/WLC band. This observation differs from that of α Leo described above only in that the star is a factor of about ten fainter in the visible and that not enough passes were done to make a measurement of $\int\int C_r \, dx dy$. Thus, instead of attempting to integrate

Item	Relative standard uncertainty (%)
positional uncertainty	10
stellar photometry	2
occulter position	0.5
$\int \cdots d\lambda$	≈ 0
Poisson statistics	≈ 0
quadrature sum	10

Table 12.2: Summary of uncertainties for the α-Leo radiometric calibration: see Equation (12.29).

something akin to the data in Figure 12.5, we multiplied the ρ-Leo integrated count-rates by ten and plotted them with the α-Leo data in Figure 12.6. Since these two data sets fall on the same curve, we take the ρ-Leo measurents as a confirmation of the validity of the α-Leo result.

12.3.4 Jupiter 2001 Radiometric Calibration

The Jupiter radiometric calibration is based on Jupiter observations taken in June 2001. This calibration accounts for both the spectral properties of Jupiter and the broad point spread function of the WLC. On 16 June 2001 Jupiter was at opposition and the angle between the Sun and Jupiter was only about 1.75° or 6 $R_\odot$, thus UVCS observed, essentially, the entire solar illuminated surface of Jupiter.

Jupiter Spectral Radiance Computation

The projected solar spectral photon irradiance hitting a surface element of Jupiter is given by the expression

$$F_{in}(\lambda) \;=\; B_\odot(\lambda)\frac{4}{5}\frac{\pi R_\odot^2}{d^2}\cos\varphi \tag{12.23}$$

where $B_\odot$ is the solar disk-center spectral radiance, d is the Sun-Jupiter distance, and φ is the angle between the normal to Jupiter's surface and the rays coming from the center of the solar disk. The 4/5 factor accounts for solar limb-darkening and the cosine factor accounts for the projection effect. Since the incoming spectral irradiance times the albedo is equal to the outgoing spectral irradiance we have

$$F_{out}(\lambda) \;=\; a(\lambda)F_{in}(\lambda) \tag{12.24}$$

where $a(\lambda)$ is the Bond albedo [*Allen*, 1976].

The relationship between F_{out} and the spectral radiance $I_J(\lambda)$ is determined by the angular distribution of the radiation. We assume that the radiance is not a function of angle [*Tejfel et al.*, 1993; *Chanover*, 2001], that is $I_J(\lambda;\theta,\phi) \;=\; I_J(\lambda)$. Then we have the relation

$$F_{out}(\lambda) \;=\; \int_0^{2\pi}\int_0^{\pi/2} I_J(\lambda)\cos\theta\,\sin\theta\,d\theta d\phi \;=\; \pi I_J(\lambda) \tag{12.25}$$

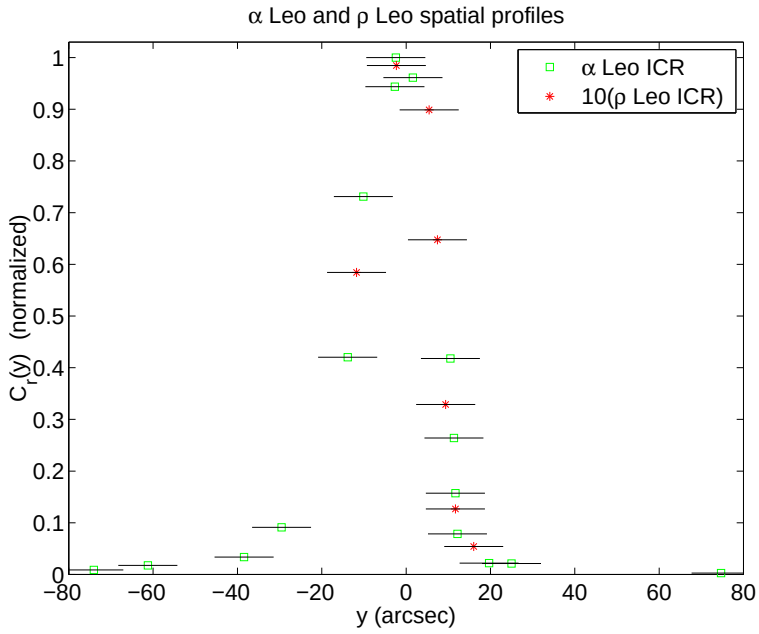

Figure 12.6: The α-Leo (squares) and ρ-Leo (asterisks) integrated count-rates along the UV slit. The ρ-Leo data have been multiplied by ten, according to the expected flux difference. Except for the factor of ten, both data sets have been normalized as in Figure 12.5. The horizontal error bars represent coverage factor $k = 2$ uncertainties. This is a confirmation of the α-Leo calibration because it gives no reason to believe that a complete data-set on ρ Leo would give an inconsistent result.

Thus, from Equations (12.23), (12.24) and (12.25) we have the following Equation

$$I_J(\lambda) \;=\; \mathrm{B}_{\odot}(\lambda) a(\lambda) \frac{4}{5} \frac{\mathrm{R}_{\odot}^2}{d^2} \cos\varphi \tag{12.26}$$

Relationship Between Spectral Radiance and the Photomultiplier Count-rate

The count-rate N (in units of s^{-1}) measured by the detector for unpolarized light of photon spectral radiance I (in units of $\mathrm{cm}^{-2}\ \mathrm{s}^{-1}\ \mathrm{nm}^{-1}\ \mathrm{sr}^{-1}$) can be derived from Equation (12.6), and is given by the Equation

$$N \;=\; R_T\ T_P\ T_L\ \frac{1}{2}\ \frac{w_p h_p h_m w_m(r)}{f^2} \int I(\lambda)\ T_F(\lambda)\ \eta(\lambda)\ \mathrm{d}\lambda \tag{12.27}$$

Since Jupiter is essentially unpolarized, the HWRP has no effect and the linear polarizer cuts the intensity in half. Therefore we have placed a factor of one-half in Equation (12.27) instead of using the polarimeter Mueller matrix. Figure 12.7 is a plot of the wavelength-dependent detected quantum responsivity, the bandpass transmittance, the Sun-center spectral radiance and the reflected Jupiter spectrum [*Karkoschka*, 1994]: all

normalized to unity at 546 nm. Using Equations (12.27) and (12.9), the relationship between the detector count-rate and the Jupiter radiance is

$$N_{\text{Jupiter}} = 2\epsilon b \frac{w_p h_p h_m w_m(r)}{f^2} \left(\int \frac{T_F(\lambda)}{T_F(\lambda_0)} \frac{\eta(\lambda)}{\eta(\lambda_0)} \frac{I_J(\lambda)}{I_J(\lambda_0)} \, \mathrm{d}\lambda \right) \frac{I_J(\lambda_0)}{2} \tag{12.28}$$

where $\lambda_0 = 546$ nm and b is an instrument broadening factor, which is the fractional reduction in the apparent center radiance due to instrument blur. The evaluation of b for Jupiter is discussed below. Note that the integral in Equation (12.28) has units of wavelength.

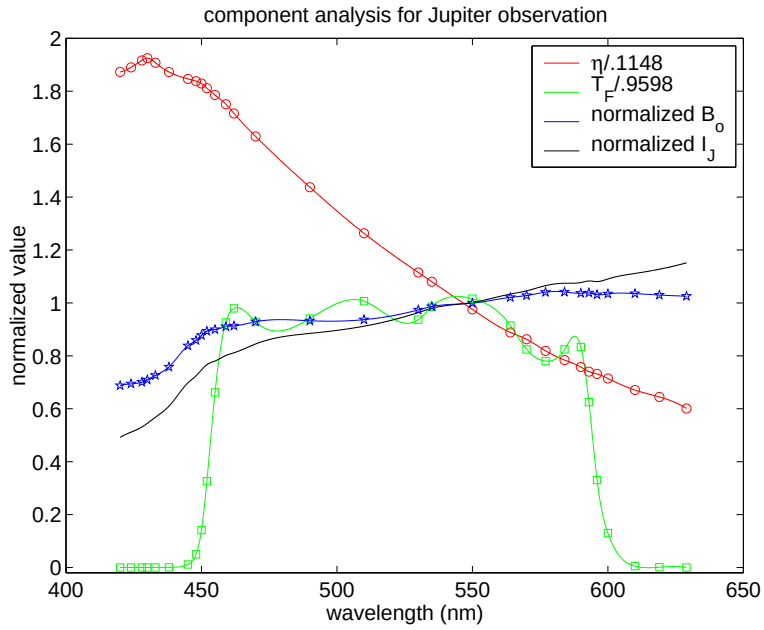

Figure 12.7: Radiometric calibration curves. Shown are the UVCS/WLC bandpass filter transmittance, the solar mean spectral radiance, the reflected Jupiter spectral radiance and the detected quantum responsivity: all normalized to unity at 546 nm.

Calibration Factor Computation

Using Equations (12.11) and (12.26), Equation (12.28) can be rewritten:

$$N_{\text{Jupiter}} = b\mathrm{K}w_m(r) \left(\frac{\int \frac{T_F(\lambda)}{T_F(\lambda_0)} \frac{\eta(\lambda)}{\eta(\lambda_0)} \frac{I_J(\lambda)}{I_J(\lambda_0)} \, \mathrm{d}\lambda}{\int \frac{T_F(\lambda)}{T_F(\lambda_0)} \frac{\eta(\lambda)}{\eta(\lambda_0)} \frac{\mathrm{B}_\odot(\lambda)}{\mathrm{B}_\odot(\lambda_0)} \, \mathrm{d}\lambda} \right) a(\lambda_0) \frac{4}{5} \frac{\mathrm{R}_\odot^2}{d^2} \cos\varphi \tag{12.29}$$

remembering that $\lambda_0 = 546$ nm; $w(r)$ is the exposed mirror width in centimeters, and K is the radiometric calibration factor defined in Section 12.2.3.

We may now use the Jupiter count-rates and Equation (12.29) to determine the value of K. The maximum Jupiter count-rate on 16 June 2001 was 1.59×10^5 s^{-1}, the mirror width

was $w_m(r) = 2.56$ cm, the ratio of the wavelength integrals is $(150.5\text{ nm})/(156\text{ nm}) = 0.965$, $a(546\text{ nm}) = 0.493$ [*Karkoschka*, 1994], $R_\odot = 6.96 \times 10^5$ km, and at that time the Sun-Jupiter distance was 7.630×10^8 km. Since the observation was essentially "straight on," we have $\cos\varphi \approx 1.0$. The value of b is shown below to be 0.72. Using these values in Equation (12.29), we find that

$$K = 2.76 \pm 0.50 \times 10^{11}\ \text{cm}^{-1}\,\text{s}^{-1} \tag{12.30}$$

This calibration factor corresponds to a radiometric responsivity of $\epsilon = (1.38 \pm 0.13)\%$. The uncertainty analysis is discussed in Section 12.3.4.

Evaluation of the Broadening Factor *b*

The UVCS/WLC telescope mirror has out-of-focus and optical aberrations that strongly affect the observations of objects that are less than about $1'$ in size. These aberrations blur the image over the pinhole so that a significant fraction of the object's light will not pass through the pinhole. Jupiter is an extended object and its angular diameter, as viewed from Earth on the observation date, is about $30''$. This substantially lessens the broadening effect (compared to stars). We determined the broadening function with observations of the star α Leo by allowing it to drift past the pinhole as described in Section 12.3.1.

To calculate the one-dimensional (1D) broadening factor and its uncertainty, we convolved the Jupiter image, given by Equation (12.26), with the profiles shown in Figure 12.5 (see Section 12.3.2). The optimal 1D broadening factor (0.77) was calculated using the solid curve. The dotted and dashed curves in that figure lead to a (coverage factor $k = 2$) 9 % relative uncertainty in this factor.

Figure 12.8 shows the effect of the convolution. The dashed curve is the ideal Jupiter image, the solid curve is the optimal profile (same as the solid curve in Figure 12.5), and the dotted curve is the result of the convolution. The convolution reduced the (normalized) peak of the Jupiter image from 1.0 to 0.77 for the case of the optimal 1D profile.

The two-dimensional (2D) point broadening function was approximated by

$$p(u, v) = p_1(u)\,p_2(v) \tag{12.31}$$

where $p_1(u)$ and $p_2(v)$ are broadening functions parallel and perpendicular to the UV slit, respectively. $p_1(u)$ is shown in Figure 12.5. $p_2(v)$ was chosen to match one of the scans of α Leo as its image passed through the center of the white-light pixel and is shown in Figure 12.9. Figure 12.9 shows that the data are well-matched by convolving the $14''$ width of the pinhole with a Gaussian optical spread function. The lower panel shows $p_2(v)$ and the pinhole and Gaussian functions that comprise it. The width of the Gaussian was varied to find a best fit to the data in the upper panel of Figure 12.9.

Comparison of Figures 12.9 and 12.5 shows that $p_2(v)$ is much narrower than $p_1(u)$. Thus, we expect the result of the 2D broadening calculation to be not much different than that of the 1D broadening calculation. Furthermore since $p_2(v)$ is narrower than $p_1(u)$ and is better constrained by the data, we can expect the uncertainty in the 2D broadening to be dominated by the uncertainty in the 1D broadening described above. Convolving $p(u, v)$ from Equation (12.31) with a 2D Jupiter image calculated from Equation (12.26) gives a 2D broadening factor of $b = 0.72$. Since Equation (12.31) is separable, the relative uncertainty in the broadening effect is still determined by the broadest and narrowest curves in Figure 12.5 and is 9 % (coverage factor $k = 2$).

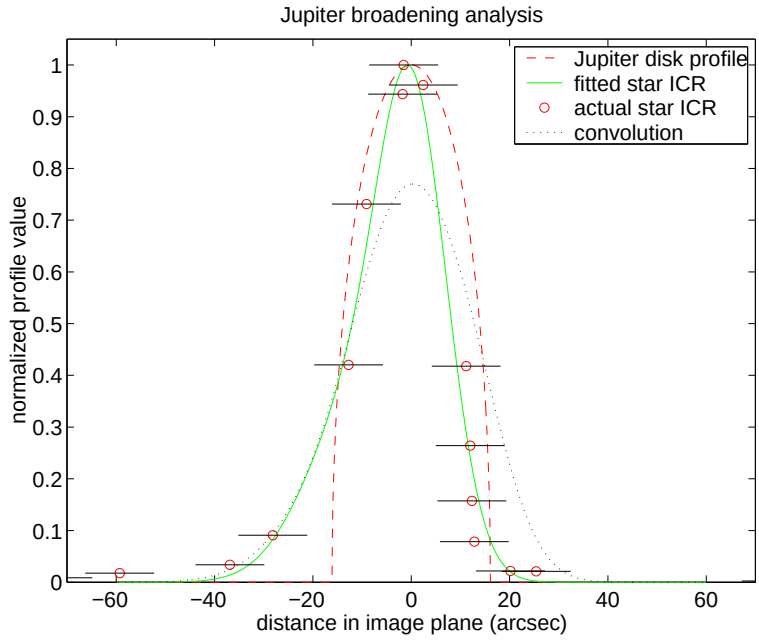

Figure 12.8: Illustration of Jupiter broadening parallel to the UV slit. The dashed curve is the Jupiter image, the solid curve is the optimal profile, and the dotted curve is the result of the convolution. Also shown in circles is the α-Leo integrated count-rate (ICR). The profiles of the Jupiter disk and α Leo have been normalized to the same peak value of unity.

Jupiter Uncertainty Analysis

The uncertainty analysis of the calibration factor K is based on Equation (12.29). The uncertainty in K is dominated by the uncertainties in the broadening factor b and the albedo a. The uncertainty in b has been discussed above. Since the 9 % relative uncertainty in b is based on a coverage factor $k = 2$ uncertainty in the spatial position of the α-Leo UV signature shown in Figure 12.5, it should also be considered roughly equivalent to a coverage factor $k = 2$ uncertainty. We will take the relative standard uncertainty to be 5 %.

Axel [1972] has compiled albedo measurements from a number of different authors, although only three measurements are within the UVCS/WLC bandpass. These albedo measurements range from 89 % to 102 % of values given by *Karkoschka* [1994]. The standard deviation of the four data sets (including Karkoschka's) is 7 %. We have adopted this value as the standard uncertainty in Jupiter's albedo. Including Karkoschka's 4 % relative standard radiometric uncertainty in quadrature, we take the overall relative standard uncertainty in Jupiter's albedo to be 8 %.

Since N_{Jupiter} was 1.59×10^5 s^{-1} and the exposure time was 15 s, the uncertainty due to Poisson statistics is negligible. Since the exposed mirror width $w_m(r)$ was 25.6 mm, and the uncertainty in the location of the internal occulter is on the order of 0.1 mm, the

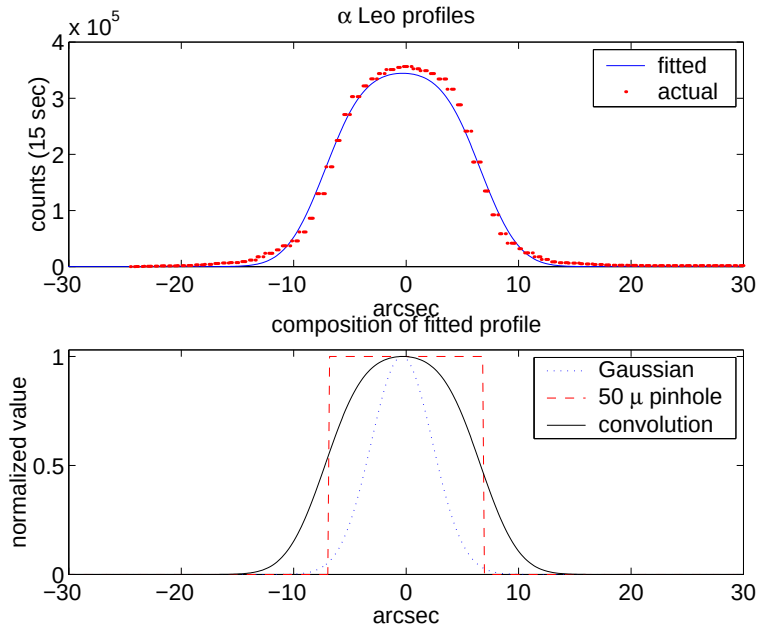

Figure 12.9: Illustration of the α-Leo image perpendicular to the UV slit length. The data in the upper panel were taken as the star passed through the center of the white-light pixel. The lower panel shows the best-fit (the width of the Gaussian was allowed to vary) composition of the fitted (solid) curve in the upper panel. The solid curves in both panels are identical.

associated uncertainty is also negligible. The ratio of the wavelength integrals would be unity, except for the slight difference between curves $I_J(\lambda)/I_J(\lambda_0)$ and $B_\odot(\lambda)/B_\odot(\lambda_0)$, which are shown in Figure 12.7. Since these curves are so similar, the uncertainty in the ratio of integrals is negligible when compared to the uncertainty in the broadening factor or the albedo. For the 2001 Jupiter observations, the uncertainty in φ may be estimated by comparing the maximum count-rates in the five Jupiter passes and fitting them to a cosine curve. The result is $\varphi < 12°$ for the central pass. Since $\cos(12°) \approx 0.978$, this uncertainty is also negligible. The solar radius $R_\odot$ is known to three or four digits (see, e.g., *Allen* [1976]) and the Sun-Jupiter distance d can be calculated to several kilometers or less. This uncertainty analysis is summarized in Table 12.3.

12.3.5 Jupiter 1997 Radiometric Calibration

The Jupiter 1997 observation was almost identical to the 2001 observation described above, and has been described in detail by *Cranmer* [2001]. The only important difference between the two observations is the way in which the instrument was pointed. Since the pointing calibration had not yet been fully established and Jupiter's position relative to the Sun not precisely calculated for the 1997 observation, the UVCS/WLC was repointed after

Parameter symbol	Parameter name	Relative standard uncertainty (%)
b	broadening parameter	5
$a(\lambda_0)$	albedo	8
$\cos\varphi$	radiation angle	2
$w_m(r)$	exposed mirror width	0.4
$N_{\text{Jupiter}}\times(15\text{ s})$	number of counts	0.065
$\int\cdots/\int\cdots$	ratio of integrals	≈ 0
$\text{R}_\odot$	solar radius	≈ 0
d	Sun-Jupiter distance	≈ 0
σ	Poisson statistics	≈ 0
quadrature sum		9.4

Table 12.3: Summary of uncertainties for the Jupiter radiometric calibration: see Equation (12.29).

every exposure in an effort to put the WLC over the center of the planet. The result was a series of exposures randomly clustered around the planet. A histogram of the resulting intensities shows a clear cut-off at a maximum intensity. We have assumed that this cut-off intensity corresponds to the WLC being pointed near the center of the disk. In contrast, the Jupiter 2001 observations were carefully rastered in a way such that the observation plan ensured that the WLC was pointed at the center of the planet at some time. Since the 2001 pointing scheme was better, we use the 2001 observations to determine our best value of the Jupiter calibration and use the 1997 observation as a confirmation.

For the 1997 Jupiter observations, all of the analysis given above for the 2001 observations carries over exactly. The result is $\epsilon = (1.33 \pm 0.13)$ %.

12.4 A Model of the Stray Light in the WLC

In Section 12.2.1 we described the procedure for computing the first three components of the Stokes vector of the light that enters the pinhole, $\boldsymbol{s}$. This light has two components, one, $\boldsymbol{s}_c$, is coronal in origin and the other, $\boldsymbol{s}_i$, is instrumental in origin. Thus, $\boldsymbol{s} = \boldsymbol{s}_c + \boldsymbol{s}_i$. In this section we describe a model of $\boldsymbol{s}_i$, so that $\boldsymbol{s}_c$ may be determined from observations of the corona.

Romoli and Reardon [2000] performed an extensive analysis of the stray-light in the WLC. The fact that the photomultiplier gave a count-rate consistent with the dark-rate when the internal occulter completely covered the mirror indicates that all of the stray-light in the WLC comes from the mirror or its edge, and not from the internal occulter surface. While the mirror-edge may scatter light from the sunlight trap, the mirror surface is only illuminated by light from the corona and light from the solar disk that has been diffracted by the external occulter. In order to determine the contribution of diffracted light to the signal, it was first necessary to measure the Stokes vector of the distribution of diffracted light across the mirror surface. This was done by pulling back the internal occulter, which allows the specularly reflected ray of the diffraction pattern to enter the pinhole, and taking polarization measurements. The Stokes vector of the resulting diffraction pattern, as a function of position along the mirror surface x is denoted by

Height ($R_\odot$)	Q_{corr}	ΔQ_{corr}
1.74	$0.6\ 10^{-8}$	$0.2\ 10^{-8}$
1.84	$0.1\ 10^{-8}$	$0.0\ 10^{-8}$
1.94	$0.7\ 10^{-9}$	$0.3\ 10^{-9}$
2.04	$0.4\ 10^{-9}$	$0.1\ 10^{-9}$
2.29	$0.7\ 10^{-10}$	$0.4\ 10^{-10}$
2.54	$0.3\ 10^{-10}$	$0.4\ 10^{-10}$
3.00	$0.4\ 10^{-10}$	$0.2\ 10^{-10}$
3.54	$0.2\ 10^{-10}$	$0.1\ 10^{-10}$
4.00	$0.2\ 10^{-10}$	$0.1\ 10^{-10}$
4.54	$0.2\ 10^{-10}$	$0.1\ 10^{-10}$
4.84	$0.2\ 10^{-10}$	$0.1\ 10^{-10}$

Table 12.4: Results of stray-light model. Q_{corr} is the number that needs to subtracted from the observed polarized radiance when nominal (1.5 mm) occulting is used. ΔQ_{corr} is the uncertainty in this quantity. These numbers are in units of Sun-center spectral radiance and assume the Jupiter 2001 radiometric calibration.

$[D(x),\ q(x)D(x),\ u(x)D(x)]^T$.

Romoli and Reardon [2000] modeled the measured Stokes parameters as:

$$\begin{aligned} I &= \frac{I_e}{w_m(r)} + I_c(r) + \frac{A_I}{w_m(r)} \int_0^{w_m(r)} D(x)\phi(x,r)\,\mathrm{d}x \\ Q &= \frac{Q_e}{w_m(r)} + Q_c(r) + \frac{A_Q}{w_m(r)} \int_0^{w_m(r)} q(x)D(x)\phi(x,r)\,\mathrm{d}x \\ U &= \frac{U_e}{w_m(r)} + \frac{A_U}{w_m(r)} \int_0^{w_m(r)} u(x)D(x)\phi(x,r)\,\mathrm{d}x \end{aligned} \tag{12.32}$$

where r is the mirror angle; $w_m(r)$ is the exposed mirror width; I_e/w_m, Q_e/w_m and U_e/w_m are the Stokes parameters of the contribution from the mirror edge; I_c, and Q_c are the Stokes parameters of the contribution from the corona (U_c is assumed to be zero, using the proper reference system), A_I, A_Q and A_U are the coefficients of non-specular scattering for the three Stokes components, and $\phi(x,r)$ is the non-specular scattering function. The parameters w_m and r are fixed by the observations and all of the other parameters are determined by the curve-fits to specially designed observations. *Romoli and Reardon* [2000] examined several options for the scattering profile $\phi(x,r)$. Based on goodness-of-fit, they chose $\phi(x,r)$ to be a Lorentzian to the power of two.

Without entering the details of the special observations that were used to determine the values of the model parameters, the model is capable of determining the stray-light contribution at every height between 1.7 $R_\odot$ and 5 $R_\odot$ and for any position of the internal occulter. The stray-light correction term is computed, for the known exposed mirror width $w_m(r)$, from

$$Q_{corr} = \frac{Q_e}{w_m(r)} + \frac{A_Q}{w_m(r)} \int_0^{w_m(r)} q(x)D(x)\phi(x,r)\,\mathrm{d}x \tag{12.33}$$

and subtracted from the measured Stokes Q.

This model has been used to calculate a value of the Stokes Q parameter that should be subtracted from coronal measurements with nominal (1.5 mm) occulting. Table 12.4 gives the stray-light correction term as a function of height.

12.5 Conclusion

We have discussed the in-flight radiometric calibration, the polarization calibration and the stray-light calibration of the UVCS White Light Channel. The in-flight radiometric calibration is based on measurements of Jupiter performed in June 2001 and of α Leo obtained in 1997. The Jupiter 2001 measurement was confirmed by a previous measurement of Jupiter in 1997 and the α-Leo measurement was confirmed by a measurement of ρ Leo. The Jupiter 2001 and α-Leo measurements agree to within the stated uncertainties.

Acknowledgements

This work is supported by NASA under grant NAG5-10093 to the Smithsonian Astrophysical Observatory, by the Italian Space Agency, and by the Prodex programme of ESA (Swiss contribution).

Bibliography

Allen, C.W., Astrophysical Quantities, London, Athlone, 1976.

Altschuler, M.D., in Image Reconstruction from Projections: Implementation and Applications, edited by G.T. Herman, New York, Springer-Verlag, 1979.

Axel, L., Inhomogeneous models of the atmosphere of Jupiter, *Astrophys. J.* **173**, 451, 1972.

Billings, D.E., A Guide to the Solar Corona, New York, Academic Press, 1966.

Breger, M., Catalog of spectrophotometric scans of stars, *Astrophys. J. Suppl.* **32**, 7, 1976.

Chanover, N., personal communication, 2001.

Collett, E., Polarized Light: fundamentals and applications, New York, Marcel Drekker, Inc., 1993.

Cranmer, S.R., unpublished technical report, 2001.

Frazin, R.A., Ph.D. Thesis. University of Illinois, Department of Astronomy, 2002.

Frazin, R.A., Romoli, M., Kohl, J.L., Gardner, L.D., Wang, D., Howard, R.A., and Kucera, T.A., White Light inter-calibrations of UVCS, LASCO and Spartan 201/WLC, this volume, 2002.

Jacoby, G. H., Hunter, D. A., and Christian, C. A., A library of stellar spectra, *Astrophys. J. Suppl.* **56**, 257, 1984.

Karkoschka, E., Spectrophotometry of the Jovian planets and Titan at 300- to 1000-nm Wavelength: The methane spectrum, *Icarus* **111**, 174, 1994.

Kohl, J.L., Esser, R., Gardner, L. D., Habbal, S., Daigneau, P. S., Dennis, E. F., Nystrom, G. U., Panasyuk, A., Raymond, J. C., Smith, P. L., Strachan, L., van Ballegooijen, A. A., Noci, G., Fineschi, S., Romoli, M., Ciaravella, A., Modigliani, A., Huber, M. C. E., Antonucci, E., Benna, C., Giordano, S., Tondello, G., Nicolosi, P., Naletto, G.,

Pernechele, C., Spadaro, D., Poletto, G., Livi, S., von der Lühe, O., Geiss, J., Timothy, J. G., Gloeckler, G., Allegra, A., Basile, G., Brusa, R., Wood, B., Siegmund, O. H. W., Fowler, W., Fisher, R., and Jhabvala, M., The Ultraviolet Coronagraph Spectrometer for the Solar and Heliospheric Observatory, *Sol. Phys.* **162**, 313, 1995.

Kurucz, R.L., Furenlid, I., Brault, J., and Testerman, L., Solar flux atlas from 296 to 1300 nm, NSO Atlas No.1, 1984.

Pernechele, C. Naletto, G., Nicolosi, P., Tondello, G., Fineschi, S., Romoli, M., Noci, G., Spadaro, D., and Kohl, J., Optical performances of the Ultraviolet Coronagraph Spectrometer of the Solar Heliospheric Observatory, *Applied Optics* **36**, 4, 813, 1997.

Romoli, M., Ph. D. thesis, The UVCS/SOHO coronagraph polarimeter, University of Florence, Department of Astronomy and Space Science, 1992.

Romoli, M., and Fineschi, S., unpublished technical report, 1993.

Romoli, M., Weiser, H., Gardner, L.D., and Kohl, J.L., Stray-light suppression in a reflecting white-light coronagraph, *Applied Optics* **32**, 3559, 1993.

Romoli, M., and Reardon, K., unpublished technical report, 2000.

Tejfel, T.G., Tejfel, V. G., Vdovichenko, V. D., Sinyaeva, N. V., Mosina, S. A., Gajsina, W. N., Kharitonova, G. A., Aksenov, A. N., Spectrophotometry of zonal cloud structure variations on Jupiter, *J. Geophys. Res.* **99**, 8411, 1994